Riley N Troyer[1], Allison N Jaynes[2], David P Hartley[2], Nigel P Meredith[3], Man Hua[4], and Jacob Bortnik[4]

[1]Affiliation not available
[2]Department of Physics and Astronomy, University of Iowa
[3]British Antarctic Survey, Natural Environment Research Council
[4]University of California

May 25, 2023

Abstract

Energetic electron precipitation (EEP) associated with pulsating aurora can transfer greater than 30 keV electrons from the outer radiation belt region into the upper atmosphere and can deplete atmospheric ozone via collisions that produce NOx and HOx molecules. Our knowledge of exactly how EEP occurs is incomplete. Previous studies have shown that pitch angle scattering between electrons and lower-band chorus waves can cause pulsating aurora associated with EEP and that substorms play an important role. In this work, we quantify the timescale of chorus wave decay following substorms and compare that to previously determined timescales. We find that the chorus decay e-folding time varies based on magnetic local time (MLT), magnetic latitude, and wave frequency. The fastest decay occurs for lower-band chorus in the 21 to 9 MLT region and compares well to the timescale of Troyer et al. (2022) for energetic pulsating aurora. We are able to further support this connection by modelling our findings in a quasi-linear diffusion simulation. These results provide observations of how chorus waves behave after substorms and add additional statistical evidence linking energetic pulsating aurora to substorm driven lower-band chorus waves.

frontiers

Substorm Driven Chorus Waves: Decay Timescales and Implications for Pulsating Aurora

Riley N. Troyer [1,*], **Allison N. Jaynes** [1], **David P. Hartley** [1], **Nigel P. Meredith** [2], **Man Hua** [3], **Jacob Bortnik** [3]

[1] *University of Iowa, Department of Physics and Astronomy, 203 Van Allen Hall, Iowa City, IA, 52242, USA*
[2] *British Antarctic Survey, Natural Environment Research Council, Cambridge, UK*
[3] *University of California, Los Angeles, Los Angeles, CA*

Correspondence*:
Corresponding Author
science@rileytroyer.com

ABSTRACT

Energetic electron precipitation (EEP) associated with pulsating aurora can transfer greater than 30 keV electrons from the outer radiation belt region into the upper atmosphere and can deplete atmospheric ozone via collisions that produce NOx and HOx molecules. Our knowledge of exactly how EEP occurs is incomplete. Previous studies have shown that pitch angle scattering between electrons and lower-band chorus waves can cause pulsating aurora associated with EEP and that substorms play an important role. In this work, we quantify the timescale of chorus wave decay following substorms and compare that to previously determined timescales. We find that the chorus decay e-folding time varies based on magnetic local time (MLT), magnetic latitude, and wave frequency. The fastest decay occurs for lower-band chorus in the 21 to 9 MLT region and compares well to the timescale of Troyer et al. (2022) for energetic pulsating aurora. We are able to further support this connection by modelling our findings in a quasi-linear diffusion simulation. These results provide observations of how chorus waves behave after substorms and add additional statistical evidence linking energetic pulsating aurora to substorm driven lower-band chorus waves.

Keywords: pulsating aurora, substorm, chorus waves

1 BACKGROUND

The outer Van Allen radiation belt is a region of space surrounding Earth, usually between $3 < L < 7$, that is filled with energetic electrons (Baker et al., 2013). These particles are trapped in the magnetic mirror created by the planet's approximate dipole magnetic field. During periods of low magnetic activity, particles are generally stably trapped and $\overrightarrow{E} \times \overrightarrow{B}$, gradient, and curvature drift around the planet (Roederer, 1970). However, there are several processes that can perturb these populations, causing them to precipitate into the atmosphere. In this study, we focus on the interaction between the energetic electrons and electromagnetic chorus waves. This interaction can precipitate energetic electrons into the atmosphere. Energetic electron precipitation (EEP) is an important dynamic to the magnetosphere-ionosphere-thermosphere coupled

system (Lam et al., 2010). It represents a significant transfer of energy from magnetosphere to upper atmosphere and can result in ozone depletion (Verronen et al., 2021; Turunen et al., 2016). Pulsating aurora is a visual manifestation of the precipitating electrons and can be an excellent way to study EEP (Bland et al., 2021). There are still many unknowns in the process that produces EEP and pulsating aurora (Lessard, 2013; Partamies et al., 2022). In this work, we provide additional statistical evidence for substorm driven lower-band chorus waves as a source of energetic pulsating aurora. We do this by measuring chorus decay e-folding times after substorms and comparing them to known pulsating aurora energy decay timescales.

Chorus waves are an important feature of the outer Van Allen radiation belt region and drive many of this regions dynamics (Meredith et al., 2020; Hua et al., 2023a,b). They are characterized by frequency, which typically ranges between the electron cyclotron frequency (f_{ce}) and one tenth of f_{ce}. There is a clear gap at one half f_{ce}, likely due to Landau resonance, such that lower-band chorus waves (LBC) occur between $0.1\ f_{ce}$ and $0.5\ f_{ce}$ while upper-band chorus waves (UBC) occur between $0.5\ f_{ce}$ and f_{ce} (Bortnik et al., 2006; Li et al., 2019). In some cases low-frequency chorus can extend to 0.05 f_{ce} or lower (Li et al., 2013; Meredith et al., 2014). For our analysis we did not consider low-frequency chorus. Chorus waves are named for their resemblance to the sound of birds chirping caused by sub-second rising and falling tones in their frequency distributions (Isted and Millington, 1957; Tsurutani and Smith, 1974). In addition to the sub-second timescales, chorus waves can also be modulated on the order of seconds (Jaynes et al., 2015). Studies have directly linked modulations over seconds in the chorus power spectral density and electron flux in the chorus region to instance of pulsating aurora, where an intensification corresponds to the brightening of an auroral patch (Nishimura et al., 2011; Jaynes et al., 2013; Kasahara et al., 2018). Due to the difficulty in connecting chorus activity to ground observations, these studies have only been able to analyze a handful of events.

Pulsating aurora are a common subset of diffuse-like aurora. They appear as an uncoordinated symphony of dim auroral patches that blink on and off across wide portions of the sky. The period of this blinking can range up to around 20 seconds. Individual patches can be remarkably varied with differing periods, shapes, and sizes typically between 10s to 100s of kilometers (Johnstone, 1978; Lessard, 2013). Pulsating aurora often develop near the end of a substorm display and can continue for hours after (Jones et al., 2011). There also is a relation between greater energy flux and closer temporal proximity to the substorm (Hosokawa and Ogawa, 2015; Oyama et al., 2017; Troyer et al., 2022). Substorms are characterized by a rapid dipolarization of Earth's nightside magnetic field that accelerates and injects electrons into the inner magnetosphere (Akasofu, 1966). Some of these electrons accelerate directly into the atmosphere, causing discrete aurora (Korth et al., 2014; Schroeder et al., 2021). Others are injected into the radiation belt region and can drive wave activity (Tsurutani and Smith, 1974; Chepuri et al., 2023). Ground-based magnetometers can detect substorms as an enhancement of the auroral electrojet and report this in the AE index (Newell and Gjerloev, 2011).

While a correlation does exist between LBC waves and pulsating aurora for certain events, it is still an open question as to how statistically significant this relationship is (Lessard, 2013; Borovsky and Partamies, 2022). That being said, there are known, indirect, statistical links between the two. For instance, both LBC and pulsating aurora occur most frequently and with the strongest intensity between 3 and 6 MLT (Oguti et al., 1981; Jones et al., 2011; Meredith et al., 2020). Additionally, pulsating aurora frequently have significant energy contributions from 10s to 100s of keV electrons, which is the resonant energy range for lower-band chorus (Nishimura et al., 2011; Tesema et al., 2020; Troyer et al., 2022). In this work we add to that evidence by showing that lower-band chorus and pulsating aurora have similar decay timescales after substorms.

A proposed process for this interaction is Doppler-shifted cyclotron resonance between 10s of keV electrons and lower-band chorus, which can simultaneously drive wave growth and pitch angle scatter electrons (Brice, 1964; Trakhtengerts et al., 2004; Miyoshi et al., 2020). Therefore, assuming pitch angle scattered electrons are responsible for pulsating aurora, a timescale in the aurora should correspond to a timescale in the waves. Troyer et al. (2022) found such a timescale for ≥ 30 keV electrons associated with pulsating aurora. They found that the differential energy flux from these electrons decayed after substorms with a timescale of just under an hour, suggesting that substorms are a primary driver of pulsating aurora EEP. Complementing this, Meredith et al. (2000) found a similar timescale when looking at post-substorm decay of chorus electric field amplitudes from the CRRES spacecraft. We hypothesize that energetic electrons injected into the outer radiation belt region during substorms drive chorus waves, and that pitch angle scattering from this interaction causes pulsating aurora. We provide evidence towards that hypothesis by expanding on Meredith et al. (2000) using the more recent and expansive Van Allen Probes dataset. In doing so, we confirmed that lower-band chorus waves decay after substorms with a similar timescale to pulsating aurora. We also discovered that this decay timescale depends on magnetic local time (MLT), magnetic latitude (MLAT), and wave frequency. Our quantified decay timescales add statistical evidence linking chorus waves, substorms, and pulsating aurora.

2 DATA

2.1 Electric and Magnetic Fields

Our primary dataset is from the Electric and Magnetic Field Instrument Suite and Integrated Science (EMFISIS) instruments aboard the Van Allen Probes. The Van Allen Probes were two identical spacecraft that orbited through the planet's radiation belt regions between 2012 and 2019 (Mauk et al., 2013). EMFISIS uses a tri-axial fluxgate magnetometer (MAG) and a tri-axial search coil magnetometer (MSC) to measure DC and wave magnetic fields respectively (Kletzing et al., 2013). EMFISIS also takes an analog electric field signal from the Electric Fields and Waves (EFW) experiment to measure the wave electric field (Wygant et al., 2013). The collective wave electric and magnetic field measurements are called the Waves experiment and cover the frequency range from 10 Hz up to 12 kHz. In survey mode, the Waves experiment provides a 6-second power spectral density for both the electric and magnetic fields in three orthogonal directions. We used the total electric/magnetic power spectral density, which is a sum of all three components.

A property of the double probe electric field sensors on the Van Allen Probes is that they become electrically coupled to the local plasma. To account for this, we use the sheath-corrected electric field measurements that provide an adjustment based on local electron density (Hartley et al., 2022). In addition, the electric field measurements contain noisy frequency bands at 1781 Hz and 3555 Hz, so we omitted this data for our analysis. We are more confident in the magnetic field measurements and used these for most of our findings.

2.2 Post-Substorm Identification

To detect substorm activity we used the SuperMAG collaboration's 1-minute SME index (Gjerloev, 2012). This index is designed to replicate the AE index using at least 100 of the SuperMAG magnetometers. Similar to AE, SME is measured in nT with larger positive values corresponding to a stronger auroral electrojet (Newell and Gjerloev, 2011).

The AE index, and thus SME, correlates well with particle injections in the inner magnetosphere (Meredith et al., 2000). These injections are linked with substorms and reconnection in the magnetotail (DeForest and McIlwain, 1971; Chepuri et al., 2023). We looked at the behavior of chorus wave events during the quiet period following an injection. We identified these events with the following process:

1. Smooth the SME index with a rolling average of 6 minutes.
2. Identify periods where the smoothed SME index stayed below 150 nT for at least 10 minutes.
3. From these periods, select only those that were preceded by an enhancement in smoothed SME of > 250 nT.

Our threshold of < 150 nT, representing the start of a quiet period, is based on Meredith et al. (2000) and we found that > 250 nT was sufficient to identify enhanced periods without over-identifying.

We also measured the approximate substorm injection period length. We define this as the time from when the smoothed SME went above 250 nT to when it dropped below 150 nT. Using this definition, our median injection length from 6241 events was 1.73 ± 0.02 hr. However, these values should be taken with a grain of salt as they assume that an enhanced SME corresponds to a continuous injection event. We've included plots of our injection period and quiet period length distributions in the supplementary materials.

2.3 Chorus Selection

Within the quiet periods after injections, we further limited our search to the outer radiation belt region ($3 \leq L \leq 6.6$) and considered all MLTs, and all magnetic latitudes sampled by the Van Allen Probes ($-20^\circ \leq \text{MLAT} \leq 20^\circ$).

To identify chorus we determined the local electron cyclotron frequency (f_{ce}) using the magnetic field amplitude from the EMFISIS flux gate magnetometer (MAG) and the equation $f_{ce}[\text{Hz}] = \left|\overrightarrow{B}[\text{nT}]\right| \times 28$. We then used local f_{ce} to select chorus from the power spectral density data. To qualify as a measurement of LBC or UBC we required that the maximum magnetic field power spectral density over the respective frequency range be $\geq 10^{-7}\text{nT}^2/\text{Hz}$ (Hartley et al., 2019). To reduce hiss noise, we ensured that the probes were outside the plasmasphere by limiting our measurements to times when the electron density was less than the smaller of $10 \times (6.6/L)^4$ or $50\,\text{cm}^{-3}$ (Lawrence et al., 1999; Sheeley et al., 2001; Aryan et al., 2022). Note that in Sheeley et al. (2001) the equation is written as $10 \times (6.6/L)^{-4}$, but we believe that this is a typograhpical mistake. Subsequent studies have implemented the equation we used to good results and it is intuitive that the density threshold would decrease at larger L values (Li et al., 2015). For the density, we used the estimated values provided by EMFISIS.

3 ANALYSIS

In total, we found 224,165 chorus measurements. Each measurement contains an integrated LBC and/or UBC wave power, probe location, and a time since the start of the respective quiet period. We can use this dataset to better understand how chorus waves behave after a substorm.

3.1 Variations with Magnetic Local Time (MLT)

We further subdivided our dataset into the following regions of MLT: 21 to 3, 3 to 6, 6 to 9, 9 to 12, 12 to 15, and 15 to 18. We excluded 18 to 21, and combined 21 to 24 and 0 to 3 due to limited chorus observations in these region. While it isn't the purpose of this study, it is worth noting that our statistical distribution does roughly agree with the previous understanding of chorus occurrence and wave power in

relation to MLT (Li et al., 2016; Meredith et al., 2020). Occurrence and wave power peaks post-midnight and are lowest between 18 and 21 MLT.

For each MLT region we performed a least squares linear fit to the natural log transformed wave power. This results in a a fitted exponential decay in form of

$$B = B_0\, e^{-t/\tau}$$

where t is the time since the start of a quiet period. We limited this fit to the first 75 minutes. Figure 1 shows how the inverse of this decay timescales (τ) varies across our MLT regions. We chose to plot $|1/\tau|$ to better distinguish between differences in decay timescales. We split the decays into full chorus (solid), LBC (dashed), and UBC (dotted) lines to visualize the differences between wave frequency. The error bars correspond to the bootstrapped standard deviation of the timescale, which we explain in Section 3.6. Using Figure 1 we find that the decay is faster in the night to early morning regions, with slower timescales on the dayside. The fastest decay occurs between 3 to 6 MLT with the LBC decaying about twice as fast as the UBC. This region of MLT also happens to be the most common region for pulsating aurora (Kvifte and Pettersen, 1969), which we will discuss in Section 3.4.

3.2 Variations with Magnetic Latitude (MLAT)

In Figure 1 we saw that decay timescales on the nightside through dawn were faster than on the dayside. To look at changes with magnetic latitude (MLAT), we divided our data into two MLT bins: 21 to 9, and 9 to 18. We would expect that close to the injection region (21 to 9 MLT), chorus would be more intense, but also damped quicker away from the equator due to the presence of Landau resonant electrons with energies on the order of 1 keV (Bortnik et al., 2007). Further away from the injection (9 to 18 MLT) we would expect less damping at higher latitudes as the $\sim$ 1 keV electrons will be lost faster than the $\sim$ 30 keV ones responsible for chorus. In Figure 2 we compare the decay timescales between these two regions and for 0° to 10° and 10° to 20° MLAT. Here the blue scatter points are the underlying data, the dashed black lines are the least squares fits to the data, and the black scatter points are the geometric mean value of the proceeding 10 minutes. We calculated the R^2 values based on the difference between the best fit line and geometric mean values. In this figure, we see that the behavior roughly agrees with what we would expect. During the daytime wave power is less intense and damped less at higher latitudes. We also see that the fastest decay occurs near the equator in the 21 to 9 MLT region. The decay time at higher latitudes is slower and not as uniform with an increase in wave power around 0.5 hours after the quiet period start. In the 9 to 18 MLT region the opposite is true. At high latitudes the decay is more uniform and faster than near the equator. Near the equator there is very little decay in wave power until around 1.25 to 1.5 hours after the quiet period start. However, the decay timescale between 1.25 and 2.5 hours is 1.57 ± 0.15 hr with an R^2 value of 0.87. We do not have a rigorous explanation for these variations, but it is interesting to note that higher latitude waves, at a given L, may originate from higher L shells near the equator (Bortnik et al., 2008). Drifts at higher L shells, for a given energy, are faster, thus could be responsible for the faster response time that we see in Panel D compared to Panel B.

3.3 Comparison with Meredith et al. (2000)

Meredith et al. (2000) used electric field measurements from the CRRES spacecraft and found a chorus amplitude decay timescale after injections of 1.1 ± 0.2 hr in the region 21 to 6 MLT and $3.8 \leq \mathrm{L} < 6$. This would correspond to a 0.55 hr decay in the wave power. To compare our data to this value we used the EMFISIS electric field measurements. We then found the electric wave power decay in the region 21

to 6 MLT, $3.8 \leq L \leq 6$, and $\pm 5^{\circ}$ MLAT, and fit our decay to the first 3 hours. Given these parameters we find that the electric wave power decays with an e-folding time of 1.20 ± 0.07 hr. This is more than double that of Meredith et al. (2000). There are a several possible reasons for this. One is the statistical sample size of they were working with < 20 data points compared to our much larger dataset. A second is the method of identifying injection periods. Our automated identification allows us to analyze the large EMFISIS dataset, but may include weaker injection periods that a human identifier would overlook. A third could be variations between our statistical sets. From Figure 3 of Meredith et al. (2000) it appears that they had the most measurements in the MLT bins around midnight, while we had comparatively few in this region. As we've seen in Figure 1, decay time is highly dependent on MLT. Thus, when averaging over a large region of MLT, differences in the statistical distribution would likely change the results.

3.4 Comparison with Pulsating Aurora and Troyer et al. (2022)

Troyer et al. (2022) found that the contribution to the total energy flux from ≥ 30 keV electrons during pulsating aurora decayed on the order of one hour after substorms. Figure 3 shows an extension of the decay plot from Troyer et al. (2022). We have fit the exponential to the underlying distribution and provided an uncertainty in the decay timescale as described in Section 3.6. In the plot, the blue scatter points are the underlying data, the black points represent the geometric mean value of the surrounding 20 minutes, and the red line is the best fit exponential. Here we see that ≥ 30 keV pulsating aurora electrons decay with an e-folding time of 0.95 ± 0.11 hr after substorms. To compare our data to these findings we considered the difference between chorus types as LBC has been directly linked to pulsating aurora, while UBC is more commonly associated with the less energetic non-pulsating diffuse aurora (Meredith et al., 2009; Nishimura et al., 2010). This is not surprising as LBC waves resonate with higher energy electrons (> 5 keV near the loss cone) compared to UBC waves (< 5 keV) (Ni et al., 2008). In Figure 1 we binned by chorus type in addition to MLT and saw that during the most common time for pulsating aurora (3 to 6 MLT), LBC decays at a faster timescale than UBC (Kvifte and Pettersen, 1969; Jones et al., 2011). For a more direct comparison to Troyer et al. (2022), in Figure 4, we show the difference between LBC and UBC in the region 21 to 5 MLT, $3 < \mathrm{L} < 6.6$, and -20° to 20° MLAT. Here we can see a clear difference between the two chorus types with LBC decaying nearly twice as quickly compared to UBC. The LBC decay is 1.07 hr to 1.29 hr considering uncertainty, compared to 0.84 hr to 1.06 hr for the ≥ 30 keV electrons from Figure 3, showing excellent consistency between the two.

3.5 Simulation

As another test, we modelled the system using the quasi-linear, drift-averaged, diffusion simulation described in Hua et al. (2022). To calculate the diffusion coefficients, we set the wave power in the 21 to 3, 3 to 6, and 6 to 9 MLT regions to

$$B_w(t) = B_0\, e^{-t/\tau}$$

where t is the simulation time, τ is the decay e-folding time that we measured for the specific region, and B_0 is the max wave intensity in the region taken from Meredith et al. (2020) at $L = 5$ and $100 \leq AE < 300$ nT. In all other regions we let $B_w(t) = B_0$.

We used the values of Meredith et al. (2020) for B_0 because they provide a large sample size over our MLT bins and have been used in similar simulations (Hua et al., 2022, 2023a). Although it wasn't the primary focus of this work, we can also derive B_0 from our data. Doing so, we find that it differs from Meredith et al. (2020). For instance, we see a peak B_0 on the order of 20 pT in the 3 to 6 MLT region, while for $AE < 100$ nT, Meredith et al. (2020) found it to be on the order of 40-50 pT. We believe this is

due to different averaging techniques. Meredith et al. (2020) used an arithmetic mean, while we used a geometric mean because the chorus power distribution is spread over multiple orders of magnitude. Using an arithmetic mean we get B_0 on the order of 40 pT.

Figure 5 summarizes the results of our simulation. Panel A shows how the initial electron energy distribution decays over the simulation. We report the electron distribution in units of spin-averaged flux as the Van Allen Probes ECT instrument would measure it (Spence et al., 2013; Boyd et al., 2019). We took the initial flux as measured by ECT from the October 25, 2016 storm event (Hua et al., 2022). In panel A we've marked the region of strong diffusion (14 keV to 125 keV) with solid black lines. We've also marked 30 keV with a dashed red line to match the threshold of Troyer et al. (2022). Panel B shows the summed electron flux, in the region of strong diffusion, for low-energy electrons (14 keV $\leq$ E $<$ 30 keV) and high-energy electrons (30 keV $\leq$ E $\leq$ 125 keV).

Due to the drift-averaged nature of the simulation, we can't directly compare these decay times to timescales measured in a specific region of MLT, although they are on the same order of magnitude. For instance, electrons with 45 keV decay the fastest with an e-folding time of 1.78 hr. This decay time will also vary depending on the peak chorus power, with higher power resulting in a faster e-folding time. We can, however, investigate the relative differences between the higher and lower energy electrons. In Figure 5B we see that, in the first 30 minutes of the simulation, the $\geq$ 30 keV electrons decay with an e-folding time of 2.04 hr, while for the $<$ 30 keV electrons the time is 4.17 hr. Clearly the flux of higher energy electrons from the radiation belt region decays at a faster rate compared to the lower energy electrons. Thus, after a substorm, we would expect to see a more dramatic change in the higher energy precipitating electrons as measured on the ground. That agrees well with Troyer et al. (2022), who showed that the post-substorm decay in energy flux during pulsating aurora was mainly due to a reduction in the $\geq$ 30 keV electrons, with the $<$ 30 keV electrons changing relatively little.

3.6 Errors

To understand the quality of our exponential fits we used two different methods. We estimated the error in τ by bootstrapping (Johnson, 2001). To bootstrap, we resampled our distribution 10,000 times, with replacement, and found the slope for these new distributions. We then used the standard deviation of these 10,000 resampled slopes as the associated error, propagating this to our timescale given that slope = -1/τ. To estimate the quality of each fit we calculated R^2 values between the best fit exponential and the geometric means values of the distribution.

4 DISCUSSION

First order cyclotron resonance with injected energetic electrons is one proposed mechanism for chorus wave growth (Brice, 1964; Kennel and Petschek, 1966). In this process the electron interacts with the perpendicular electric field, causing it to transfer energy to the wave and reducing the pitch angle. To keep wave growth active the average velocity of the electrons perpendicular to the magnetic field must be greater than the average parallel velocity (Brice, 1964). Qualitatively, our results are consistent with this process. During injections, electrons typically enter the outer radiation belt region just before magnetic midnight (Gabrielse et al., 2014). They then gradient-curvature drift eastward, overtaking the slower, less energetic (a few to $\sim$ 30 keV) plasmasheet electrons. The interaction of these two populations can provide the anisotropies necessary for pitch angle scattering (Oguti, 1976). As time progresses the electron distribution, and correspondingly wave activity, will tend towards an equilibrium Kennel and Petschek (1966). Thus, chorus wave activity should have less time dependence further eastward (later MLT). This is what we see

in Figure 1, with the fastest decay timescales between 3 to 6 MLT and the slowest timescales in later MLT bins.

Performing a quantitative analysis of the decay timescale is more challenging and not something we attempt in this paper. To do so we would need to take several aspects of the system into consideration. One is the energy dispersion due to gradient-curvature drift. Higher energy electrons will drift eastward at a faster rate, meaning the lower energy electrons will last longer in a particular MLT region. A second is the energy and pitch angle distribution of the injected electrons. The process that drives chorus growth simultaneously reduces the electron energy and pitch angle. After enough interactions an electron that was originally resonant will either precipitate into the atmosphere or lose enough energy that it is no longer resonant. A third is the temporal and spatial scale of the injection. For a longer and wider injection, by the time we take our measurement, the electron population will be spread over a larger region of MLT. We were able to estimate the median length of the injections as 1.73 ± 0.02 hours, but have no measure of the spatial extent. In Section 3.5 we were able to simulate an approximation of these events, but to understand the underlying physics we would need to specifically model the processes just after a substorm. While we did not perform that analysis, we hope that our measured decay timescales will provide a means to test future models.

The decay timescale similarity between LBC in the 21 to 5 MLT region and the energy flux of energetic pulsating aurora is striking, but also not a smoking gun. Our results should be considered as additional statistical evidence linking energetic pulsating aurora to LBC and substorms. Combined with prior studies, LBC certainly appear to play an important role in the formation of pulsating aurora, but the specific processes are likely more complicated than we've outlined here.

4.1 Magnetic and Electric Field Differences

To compare with Meredith et al. (2000) we also analysed the electric wave power for our chorus measurements. Due to data quality, we believe the magnetic field analysis is more reliable and so chose to focus on it for our results. However, during our analysis, we did find several differences between the magnetic and electric decay timescales. The largest difference was in the region 21 to 3 MLT, where $\tau_{\text{electric}} < \tau_{\text{magnetic}}$, and for 3 to 6 MLT, where $\tau_{\text{electric}} > \tau_{\text{magnetic}}$. We've included a plot showing this in the supplementary materials. We do not fully understand how this would occur, but there are a couple possibilities. One is wave normal angle of the chorus that, as Li et al. (2016) found, varies with MLT. Waves in the 3 to 6 MLT region are less field aligned (larger wave normal angle) than those close to midnight. They also found that waves with angles $> 40^\circ$ tend to have weaker magnetic field power compared with angles $< 30^\circ$, while the electric field is comparable. However, this connection is highly speculative and we would need to conduct additional work to determine if it could cause our observed decay timescale differences.

5 SUMMARY

We found that chorus waves exponentially decay in the quiet period following a substorm. The timescale of this decay varies based on magnetic local time (MLT), magnetic latitude, and frequency range. The fastest decay times occurred for lower-band chorus waves between 21 to 9 MLT with a peak at 3 to 6 MLT. The lower-band chorus magnetic field power spectral density decays in the region 21 to 5 MLT with an e-folding time of 1.18 ± 0.11 hr. This compares well with the 0.95 ± 0.11 hr timescale that Troyer et al. (2022) measured for ≥ 30 keV pulsating aurora electrons after substorms. We also modeled our findings in a quasi-linear diffusion simulation and found that ≥ 30 keV electrons decay around twice as fast compared

to the < 30 keV population. These statistical decay timescales provide a valuable metric that can be used to track processes through the magnetosphere-ionosphere system and to test the validity of future models.

CONFLICT OF INTEREST STATEMENT

The authors declare that the research was conducted in the absence of any commercial or financial relationships that could be construed as a potential conflict of interest.

AUTHOR CONTRIBUTIONS

RNT wrote the manuscript and performed the data analysis for the study. ANJ helped edit the manuscript and provided feedback and advise for the data analysis. DPH helped with the chorus wave analysis. NPM provided advice and suggestions as well as clarification of Meredith et al. (2000). MH and JB ran the quasi-linear diffusion simulation.

FUNDING

RNT was supported by the NASA FINESST award 80NSSC20K1514 to the University of Iowa.

ANJ was supported by NSF CAREER grant 2045016 to the University of Iowa.

ACKNOWLEDGMENTS

We gratefully acknowledge the SuperMAG collaborators (`https://supermag.jhuapl.edu/info/?page=acknowledgement`)

We acknowledge the Van Allen Probes mission, particularly the ECT team for providing the particle data and the EMFISIS team for providing the wave data.

JB and MH would like to gratefully acknowledge NSF/GEM award number 2225613, subcontract to UCLA through the University of Iowa.

NM would like to acknowledge funding from the Natural Environment Research Council grants NE/V00249X/1 (Sat-Risk) and NE/R016038/1

DATA AVAILABILITY STATEMENT

The Van Allen Probe/EMFISIS data referenced in this paper is available at: `https://emfisis.physics.uiowa.edu/data/index`

The SME index referenced in this paper is available from SuperMAG: `https://supermag.jhuapl.edu/indices/?fidelity=low&layers=SME.UL&start=2001-01-01T00%3A00%3A00.000Z&step=14400&tab=download`

REFERENCES

Akasofu, S.-I. (1966). The auroral oval, the auroral substorm, and their relations with the internal structure of the magnetosphere. *Planetary and Space Science* 14, 587–595. doi:10.1016/0032-0633(66)90043-2

Aryan, H., Bortnik, J., Sibeck, D. G., and Hospodarsky, G. (2022). Global Map of Chorus Wave Sizes in the Inner Magnetosphere. *Journal of Geophysical Research: Space Physics* 127. doi:10.1029/2021JA029768

Baker, D. N., Kanekal, S. G., Hoxie, V. C., Henderson, M. G., Li, X., Spence, H. E., et al. (2013). A Long-Lived Relativistic Electron Storage Ring Embedded in Earth's Outer Van Allen Belt. *Science* 340, 186–190. doi:10.1126/science.1233518

Bland, E., Tesema, F., and Partamies, N. (2021). D-region impact area of energetic electron precipitation during pulsating aurora. *Annales Geophysicae* 39, 135–149. doi:10.5194/angeo-39-135-2021

Borovsky, J. E. and Partamies, N. (2022). What produces and what controls the spatial-temporal structuring of the magnetospheric chorus waves that create the pulsating aurora: An unsolved problem in need of new measurements. *Frontiers in Astronomy and Space Sciences* 9, 1059039. doi:10.3389/fspas.2022.1059039

Bortnik, J., Inan, U. S., and Bell, T. F. (2006). Landau damping and resultant unidirectional propagation of chorus waves. *Geophysical Research Letters* 33, L03102. doi:10.1029/2005GL024553

Bortnik, J., Thorne, R. M., and Meredith, N. P. (2007). Modeling the propagation characteristics of chorus using CRRES suprathermal electron fluxes: PROPAGATION CHARACTERISTICS OF CHORUS. *Journal of Geophysical Research: Space Physics* 112, n/a–n/a. doi:10.1029/2006JA012237

Bortnik, J., Thorne, R. M., and Meredith, N. P. (2008). The unexpected origin of plasmaspheric hiss from discrete chorus emissions. *Nature* 452, 62–66. doi:10.1038/nature06741

Boyd, A. J., Reeves, G. D., Spence, H. E., Funsten, H. O., Larsen, B. A., Skoug, R. M., et al. (2019). RBSP-ECT Combined Spin-Averaged Electron Flux Data Product. *Journal of Geophysical Research: Space Physics* 124, 9124–9136. doi:10.1029/2019JA026733

Brice, N. (1964). Fundamentals of very low frequency emission generation mechanisms. *Journal of Geophysical Research* 69, 4515–4522. doi:10.1029/JZ069i021p04515

Chepuri, S. N. F., Jaynes, A. N., Turner, D. L., Gabrielse, C., Baker, D. N., Mauk, B. H., et al. (2023). A comparison of energetic particle energization observations MMS at and injections at Van Allen Probes. *Frontiers in Astronomy and Space Sciences* 9, 1033546. doi:10.3389/fspas.2022.1033546

DeForest, S. E. and McIlwain, C. E. (1971). Plasma Clouds in the Magnetosphere. *Journal of Geophysical Research* 76, 3587–3611. doi:10.1029/ja076i016p03587

Gabrielse, C., Angelopoulos, V., Runov, A., and Turner, D. L. (2014). Statistical characteristics of particle injections throughout the equatorial magnetotail. *Journal of Geophysical Research: Space Physics* 119, 2512–2535. doi:10.1002/2013JA019638

Gjerloev, J. W. (2012). The SuperMAG data processing technique. *Journal of Geophysical Research: Space Physics* 117, n/a–n/a. doi:10.1029/2012JA017683

Hartley, D. P., Christopher, I. W., Kletzing, C. A., Kurth, W. S., Santolik, O., Kolmasova, I., et al. (2022). Quantifying the Sheath Impedance of the Electric Double Probe Instrument on the Van Allen Probes. *Journal of Geophysical Research: Space Physics* 127. doi:10.1029/2022JA030369

Hartley, D. P., Kletzing, C. A., Chen, L., Horne, R. B., and Santolík, O. (2019). Van Allen Probes Observations of Chorus Wave Vector Orientations: Implications for the Chorus-to-Hiss Mechanism. *Geophysical Research Letters* 46, 2337–2346. doi:10.1029/2019GL082111

Hosokawa, K. and Ogawa, Y. (2015). Ionospheric variation during pulsating aurora. *Journal of Geophysical Research: Space Physics* 120, 5943–5957. doi:10.1002/2015JA021401

Hua, M., Bortnik, J., Kellerman, A. C., Camporeale, E., and Ma, Q. (2023a). Ensemble Modeling of Radiation Belt Electron Acceleration by Chorus Waves: Dependence on Key Input Parameters. *Space Weather* doi:10.1029/2022SW003234

Hua, M., Bortnik, J., and Ma, Q. (2022). Upper Limit of Outer Radiation Belt Electron Acceleration Driven by Whistler-Mode Chorus Waves. *Geophysical Research Letters* 49. doi:10.1029/2022GL099618

Hua, M., Bortnik, J., Spence, H. E., and Reeves, G. D. (2023b). Testing the key processes that accelerate outer radiation belt relativistic electrons during geomagnetic storms. *Frontiers in Astronomy and Space Sciences* 10, 1168636. doi:10.3389/fspas.2023.1168636

Isted, G. A. and Millington, G. (1957). The 'Dawn Chorus' in Radio Observations. *Nature* 180, 716–716. doi:10.1038/180716a0

Jaynes, A. N., Lessard, M. R., Rodriguez, J. V., Donovan, E., Loto'aniu, T. M., and Rychert, K. (2013). Pulsating auroral electron flux modulations in the equatorial magnetosphere. *Journal of Geophysical Research: Space Physics* 118, 4884–4894. doi:10.1002/jgra.50434

Jaynes, A. N., Lessard, M. R., Takahashi, K., Ali, A. F., Malaspina, D. M., Michell, R. G., et al. (2015). Correlated Pc4–5 ULF waves, whistler-mode chorus, and pulsating aurora observed by the Van Allen Probes and ground-based systems. *Journal of Geophysical Research: Space Physics* 120, 8749–8761. doi:10.1002/2015JA021380

Johnson, R. W. (2001). An Introduction to the Bootstrap. *Teaching Statistics* 23, 49–54. doi:10.1111/1467-9639.00050

Johnstone, A. D. (1978). Pulsating aurora. *Nature* 274, 119–126. doi:10.1038/274119a0

Jones, S. L., Lessard, M. R., Rychert, K., Spanswick, E., and Donovan, E. (2011). Large-scale aspects and temporal evolution of pulsating aurora. *Journal of Geophysical Research: Space Physics* 116. doi:10.1029/2010JA015840

Kasahara, S., Miyoshi, Y., Yokota, S., Mitani, T., Kasahara, Y., Matsuda, S., et al. (2018). Pulsating aurora from electron scattering by chorus waves. *Nature* 554, 337–340. doi:10.1038/nature25505

Kennel, C. F. and Petschek, H. E. (1966). Limit on stably trapped particle fluxes. *Journal of Geophysical Research* 71, 1–28. doi:10.1029/JZ071i001p00001

Kletzing, C. A., Kurth, W. S., Acuna, M., MacDowall, R. J., Torbert, R. B., Averkamp, T., et al. (2013). The Electric and Magnetic Field Instrument Suite and Integrated Science (EMFISIS) on RBSP. *Space Science Reviews* 179, 127–181. doi:10.1007/s11214-013-9993-6

Korth, H., Zhang, Y., Anderson, B. J., Sotirelis, T., and Waters, C. L. (2014). Statistical relationship between large-scale upward field-aligned currents and electron precipitation: Current-precipitation relationship. *Journal of Geophysical Research: Space Physics* 119, 6715–6731. doi:10.1002/2014JA019961

Kvifte, G. and Pettersen, H. (1969). Morphology of the pulsating aurora. *Planetary and Space Science* 17, 1599–1607. doi:10.1016/0032-0633(69)90148-2

Lam, M. M., Horne, R. B., Meredith, N. P., Glauert, S. A., Moffat-Griffin, T., and Green, J. C. (2010). Origin of energetic electron precipitation >30 keV into the atmosphere. *Journal of Geophysical Research: Space Physics* 115, n/a–n/a. doi:10.1029/2009JA014619

Lawrence, D. J., Thomsen, M. F., Borovsky, J. E., and McComas, D. J. (1999). Measurements of early and late time plasmasphere refilling as observed from geosynchronous orbit. *Journal of Geophysical Research* 104, 14691–14704. doi:10.1029/1998ja900087

Lessard, M. R. (2013). A Review of Pulsating Aurora. *Geophysical Monograph Series* , 55–68doi:10.1029/2011GM001187

Li, J., Bortnik, J., An, X., Li, W., Angelopoulos, V., Thorne, R. M., et al. (2019). Origin of two-band chorus in the radiation belt of Earth. *Nature Communications* 10, 4672. doi:10.1038/s41467-019-12561-3

Li, W., Ma, Q., Thorne, R. M., Bortnik, J., Kletzing, C. A., Kurth, W. S., et al. (2015). Statistical properties of plasmaspheric hiss derived from Van Allen Probes data and their effects on radiation belt electron dynamics. *Journal of Geophysical Research: Space Physics* 120, 3393–3405. doi:10.1002/2015JA021048

Li, W., Santolik, O., Bortnik, J., Thorne, R. M., Kletzing, C. A., Kurth, W. S., et al. (2016). New chorus wave properties near the equator from Van Allen Probes wave observations. *Geophysical Research Letters* 43, 4725–4735. doi:10.1002/2016GL068780

Li, W., Thorne, R. M., Bortnik, J., Reeves, G. D., Kletzing, C. A., Kurth, W. S., et al. (2013). An unusual enhancement of low-frequency plasmaspheric hiss in the outer plasmasphere associated with substorm-injected electrons: AMPLIFICATION OF LOW-FREQUENCY HISS. *Geophysical Research Letters* 40, 3798–3803. doi:10.1002/grl.50787

Mauk, B., N. J. Fox, Fox, N. J., Kanekal, S., Kessel, R., Sibeck, D. G., et al. (2013). Science Objectives and Rationale for the Radiation Belt Storm Probes Mission. *Space Science Reviews* 179, 3–27. doi:10.1007/s11214-012-9908-y

Meredith, N. P., Horne, R. B., Johnstone, A. D., and Anderson, R. R. (2000). The temporal evolution of electron distributions and associated wave activity following substorm injections in the inner magnetosphere. *Journal of Geophysical Research: Space Physics* 105, 12907–12917. doi:10.1029/2000JA900010

Meredith, N. P., Horne, R. B., Li, W., Thorne, R. M., and Sicard-Piet, A. (2014). Global model of low-frequency chorus ($f_{\mathrm{lhr}} < f < 0.1 f_{\mathrm{ce}}$) from multiple satellite observations. *Geophysical Research Letters* 41, 280–286. doi:10.1002/2013GL059050

Meredith, N. P., Horne, R. B., Shen, X., Li, W., and Bortnik, J. (2020). Global Model of Whistler Mode Chorus in the Near-Equatorial Region ($|\lambda_m| < 18°$). *Geophysical Research Letters* 47. doi:10.1029/2020GL087311

Meredith, N. P., Horne, R. B., Thorne, R. M., and Anderson, R. R. (2009). Survey of upper band chorus and ECH waves: Implications for the diffuse aurora. *Journal of Geophysical Research: Space Physics* 114, n/a–n/a. doi:10.1029/2009JA014230

Miyoshi, Y., Saito, S., Kurita, S., Asamura, K., Hosokawa, K., Sakanoi, T., et al. (2020). Relativistic Electron Microbursts as High-Energy Tail of Pulsating Aurora Electrons. *Geophysical Research Letters* 47. doi:10.1029/2020GL090360

Newell, P. T. and Gjerloev, J. W. (2011). Evaluation of SuperMAG auroral electrojet indices as indicators of substorms and auroral power. *Journal of Geophysical Research: Space Physics* 116, 2011JA016779. doi:10.1029/2011JA016779

Ni, B., Thorne, R. M., Shprits, Y. Y., and Bortnik, J. (2008). Resonant scattering of plasma sheet electrons by whistler-mode chorus: Contribution to diffuse auroral precipitation. *Geophysical Research Letters* 35, L11106. doi:10.1029/2008GL034032

Nishimura, Y., Bortnik, J., Li, W., Thorne, R. M., Chen, L., Lyons, L. R., et al. (2011). Multievent study of the correlation between pulsating aurora and whistler mode chorus emissions. *Journal of Geophysical Research: Space Physics* 116, n/a–n/a. doi:10.1029/2011JA016876

Nishimura, Y., Bortnik, J., Li, W., Thorne, R. M., Lyons, L. R., Angelopoulos, V., et al. (2010). Identifying the Driver of Pulsating Aurora. *Science* 330, 81–84. doi:10.1126/science.1193186

Oguti, T. (1976). recurrent auroral patterns. *Journal of Geophysical Research* 81, 1782–1786. doi:10.1029/JA081i010p01782

Oguti, T., Kokubun, S., Hayashi, K., Tsuruda, K., Machida, S., Kitamura, T., et al. (1981). Statistics of pulsating auroras on the basis of all-sky TV data from five stations. I. Occurrence frequency. *Canadian Journal of Physics* 59, 1150–1157. doi:10.1139/p81-152

Oyama, S., Kero, A., Rodger, C. J., Clilverd, M. A., Miyoshi, Y., Partamies, N., et al. (2017). Energetic electron precipitation and auroral morphology at the substorm recovery phase. *Journal of Geophysical Research: Space Physics* 122, 6508–6527. doi:10.1002/2016JA023484

Partamies, N., Tesema, F., and Bland, E. (2022). Appearance and Precipitation Characteristics of High-Latitude Pulsating Aurora. *Frontiers in Astronomy and Space Sciences* 9, 923396. doi:10.3389/fspas.2022.923396

Roederer, J. G. (1970). *Dynamics of Geomagnetically Trapped Radiation*, vol. 2 of *Physics and Chemistry in Space* (Berlin, Heidelberg: Springer Berlin Heidelberg). doi:10.1007/978-3-642-49300-3

Schroeder, J. W. R., Howes, G. G., Kletzing, C. A., Skiff, F., Carter, T. A., Vincena, S., et al. (2021). Laboratory measurements of the physics of auroral electron acceleration by Alfvén waves. *Nature Communications* 12, 3103. doi:10.1038/s41467-021-23377-5

Sheeley, B. W., Moldwin, M. B., Rassoul, H. K., and Anderson, R. R. (2001). An empirical plasmasphere and trough density model: CRRES observations. *Journal of Geophysical Research: Space Physics* 106, 25631–25641. doi:10.1029/2000JA000286

Spence, H. E., Reeves, G. D., Baker, D. N., Blake, J. B., Bolton, M., Bourdarie, S., et al. (2013). Science Goals and Overview of the Radiation Belt Storm Probes (RBSP) Energetic Particle, Composition, and Thermal Plasma (ECT) Suite on NASA's Van Allen Probes Mission. *Space Science Reviews* 179, 311–336. doi:10.1007/s11214-013-0007-5

Tesema, F., Partamies, N., Tyssøy, H. N., Kero, A., and Smith-Johnsen, C. (2020). Observations of Electron Precipitation During Pulsating Aurora and Its Chemical Impact. *Journal of Geophysical Research: Space Physics* 125. doi:10.1029/2019JA027713

Trakhtengerts, V. Y., Demekhov, A. G., Titova, E. E., Kozelov, B. V., Santolik, O., Gurnett, D., et al. (2004). Interpretation of Cluster data on chorus emissions using the backward wave oscillator model. *Physics of Plasmas* 11, 1345–1351. doi:10.1063/1.1667495

Troyer, R. N., Jaynes, A. N., Kaeppler, S. R., Varney, R. H., Reimer, A. S., and Jones, S. L. (2022). Substorm activity as a driver of energetic pulsating aurora. *Frontiers in Astronomy and Space Sciences* 9. doi:10.3389/fspas.2022.1032552

Tsurutani, B. T. and Smith, E. J. (1974). Postmidnight chorus: A substorm phenomenon. *Journal of Geophysical Research* 79, 118–127. doi:10.1029/JA079i001p00118

Turunen, E., Kero, A., Verronen, P. T., Miyoshi, Y., Oyama, S., and Saito, S. (2016). Mesospheric ozone destruction by high-energy electron precipitation associated with pulsating aurora. *Journal of Geophysical Research: Atmospheres* 121. doi:10.1002/2016JD025015

Verronen, P. T., Kero, A., Partamies, N., Szeląg, M. E., Oyama, S.-I., Miyoshi, Y., et al. (2021). Simulated seasonal impact on middle atmospheric ozone from high-energy electron precipitation related to pulsating aurorae. *Annales Geophysicae* 39, 883–897. doi:10.5194/angeo-39-883-2021

Wygant, J. R., Bonnell, J. W., Goetz, K., Keith Goetz, Ergun, R., Mozer, F. S., et al. (2013). The Electric Field and Waves Instruments on the Radiation Belt Storm Probes Mission. *Springer US* doi:10.1007/s11214-013-0013-7

FIGURES

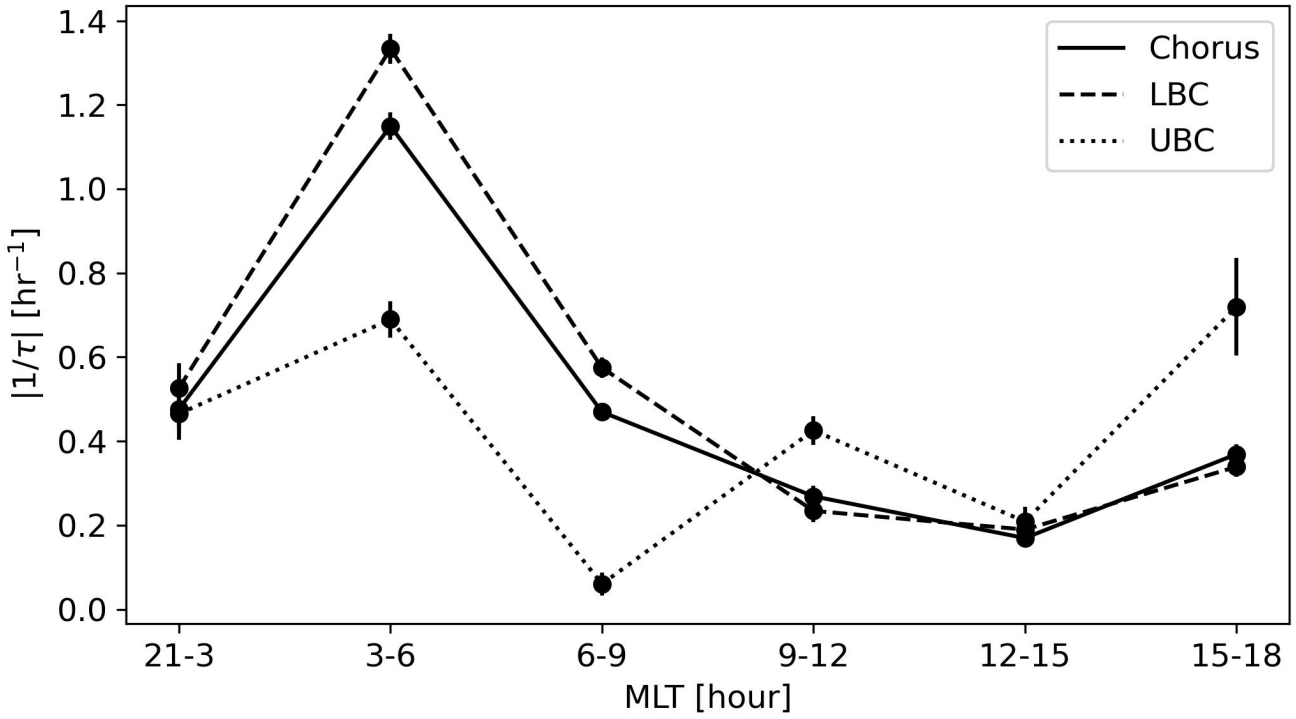

Figure 1. The inverse of magnetic field wave power decay timescales for the entire chorus range (solid), LBC (dashed), and UBC (dotted) versus MLT. For many of the points, the associated errors are smaller than the marker size. We combined the region 21 to 24 and 0 to 3 MLT and omitted 18 to 21 MLT due to statistical limitations.

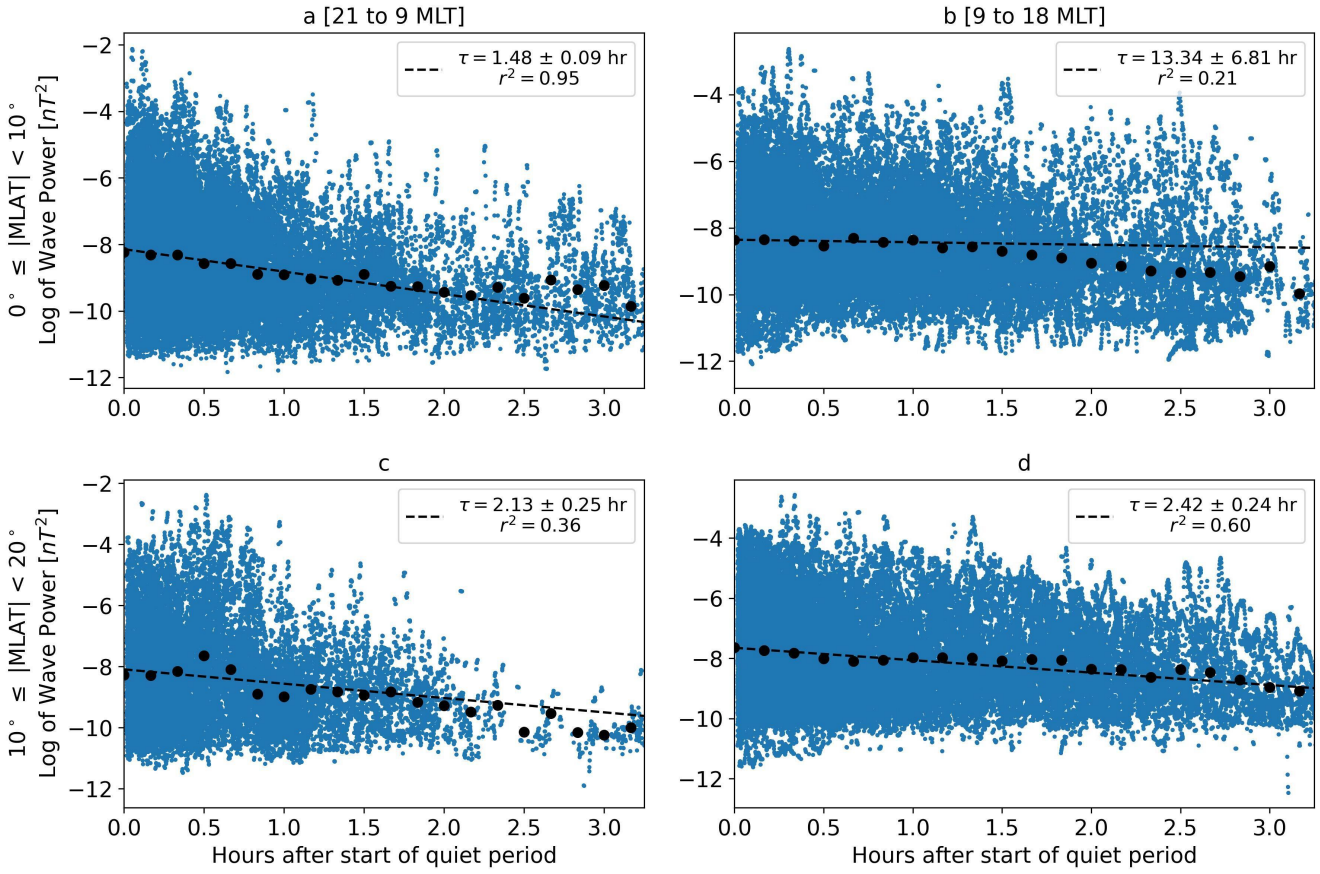

Figure 2. Statistical behavior, during the quiet period following substorms, of magnetic chorus wave power. The left (right) column of figures shows the behavior in the 21 to 9 MLT (9 to 18 MLT) region. The top (bottom) row of figures shows the behavior for 0° to 10° (10° to 20°) MLAT. The blue scatter points are the underlying data, the black scatter points are the geometric mean value of the proceeding 10 minutes of data. The dashed line is the best exponential decay to the first 75 minutes of data. Note that the wave power is natural log transformed.

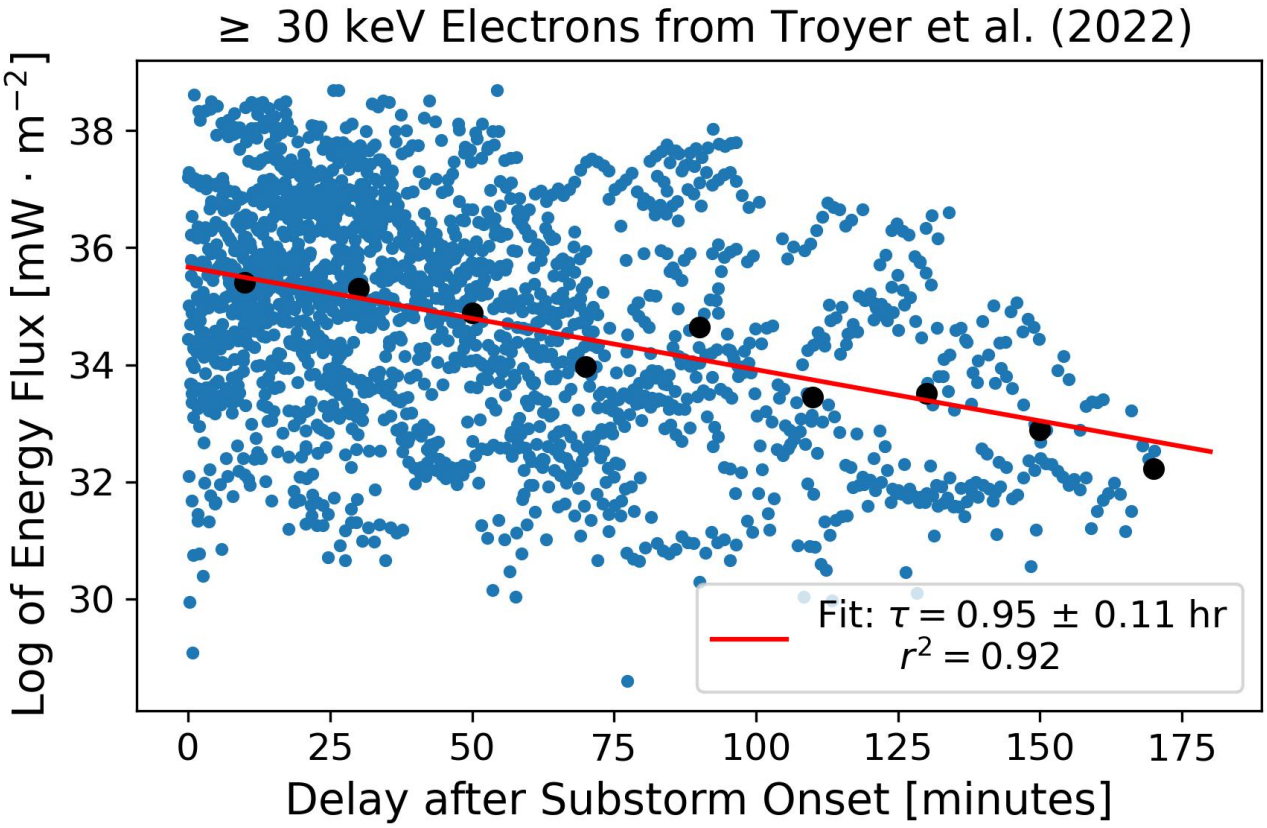

Figure 3. Updated figure from Troyer et al. (2022) showing the decay of $\geq$ 30 keV pulsating aurora electrons after substorms. The blue scatter points indicate the underlying data, the black scatter points are the geometric mean values of the surrounding 20 minutes of energy flux, and the red line is the best fit exponential decay. The r^2 value is based on the fit to the black scatter points. Note that the energy flux is natural log transformed.

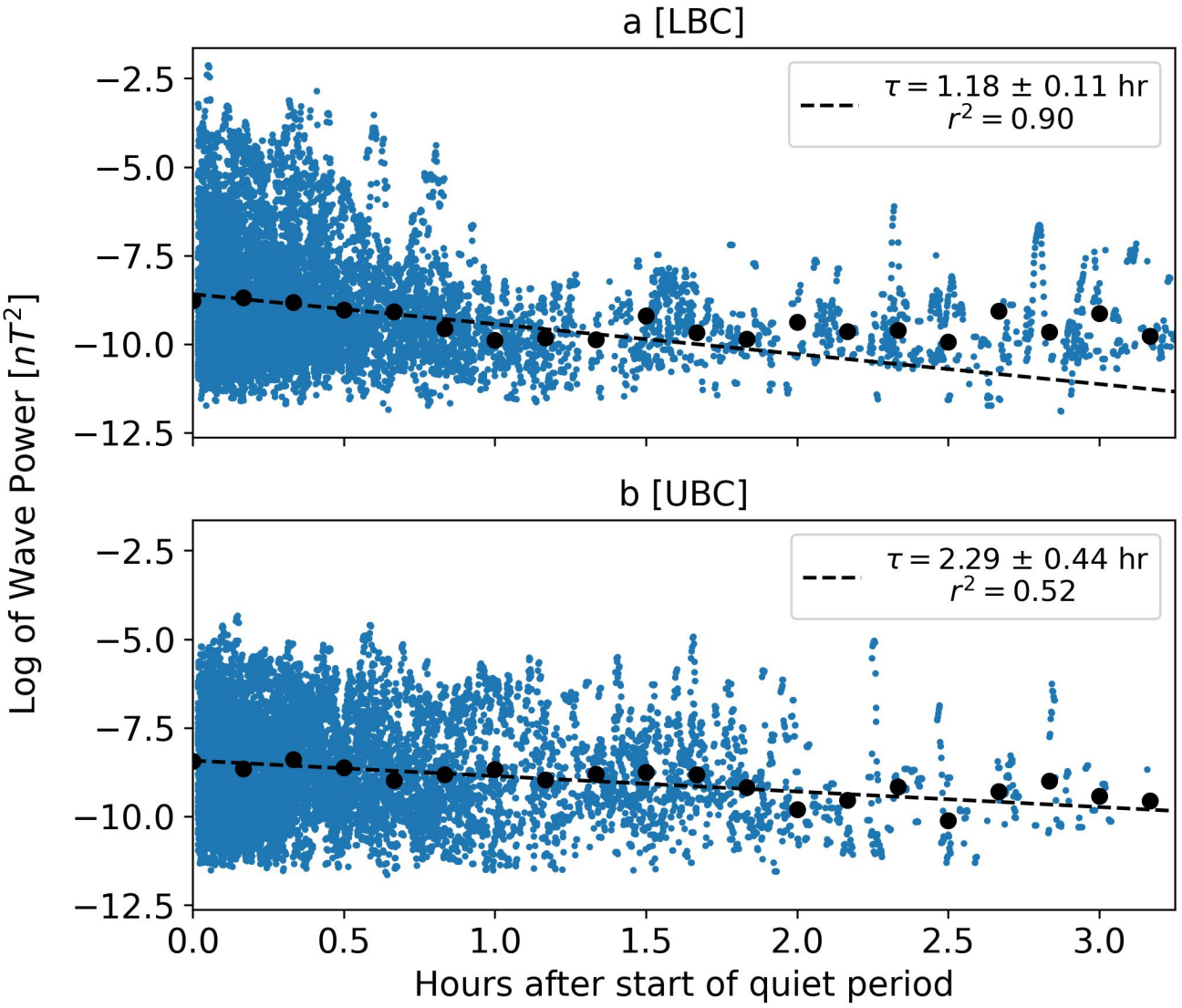

Figure 4. Statistical behavior of magnetic wave power, during the quiet period following substorms, from the LBC [a] and UBC [b] frequency ranges. Data in the figure is from the region 21 to 5 MLT, $3 < \mathrm{L} < 6.6$, and -20° to 20° MLAT. The blue scatter points indicate the underlying data, the black scatter points are the geometric mean value of the proceeding 10 minutes of data. The dashed black line is the best exponential decay to the first 75 minutes of data. Note that the wave power is natural log transformed.

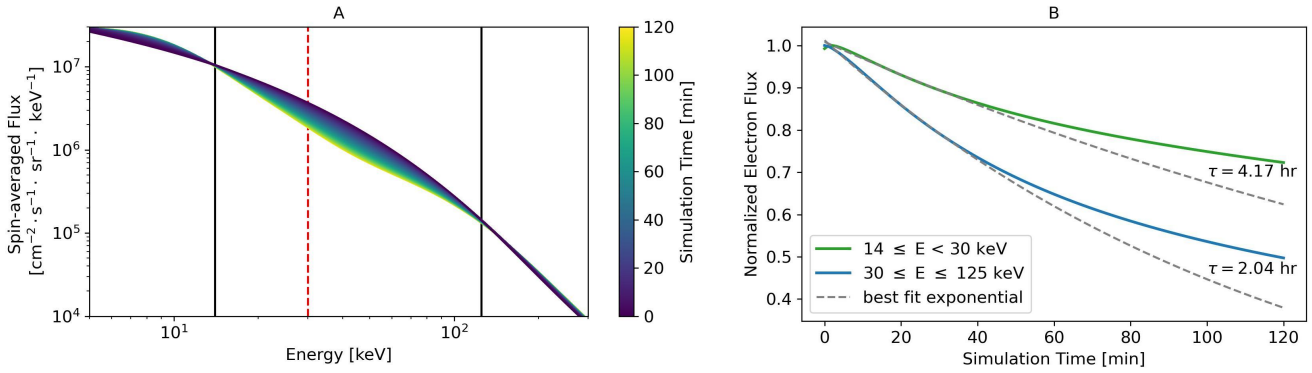

Figure 5. Results from our quasi-linear diffusion simulation of chorus waves. Panel A shows how the initial electron energy distribution decays over the simulation. The solid black lines indicate 14 keV and 125 keV and are the approximate bounds of strong diffusion. The dashed red line indicates 30 keV, which we define as the boundary between high and low energy electrons. Panel B shows the summed decay of low (14 keV $\leq$ E $<$ 30 keV) and high (30 keV $\leq$ E $\leq$ 125 keV) electrons within the region of strong diffusion. The solid lines indicate the normalized flux decays, while the dashed gray lines are the best fit exponentials for the first 30 minutes of the simulation.

Supplementary Material

1 SUPPLEMENTARY TABLES AND FIGURES

1.1 Tables

Table S1. Full chorus, LBC, and UBC magnetic (B) and electric (E) power spectral density decay timescales (τ) and peak wave magnetic field (B_w) for the midnight (21 to 3 MLT) region. We included error, R^2 values, and the number of statistics for the magnetic field measurements (N_B) to contextualize the quality of each fit.

Type	τ_B	B_w	R^2_B	τ_E	R^2_E	N_B
Chorus	2.10 ± 0.43 hr	15.2 pT	0.85	0.73 ± 0.07 hr	0.61	12123
LBC	1.90 ± 0.43 hr	11.9 pT	0.70	1.00 ± 0.20 hr	0.80	7780
UBC	2.15 ± 0.57 hr	15.9 pT	0.57	0.97 ± 0.15 hr	0.18	6862

Table S2. Full chorus, LBC, and UBC magnetic (B) and electric (E) power spectral density decay timescales (τ) and peak wave magnetic field (B_w) for the predawn (3 to 6 MLT) region. We included error, R^2 values, and the number of statistics for the magnetic field measurements (N_B) to contextualize the quality of each fit.

Type	τ_B	B_w	R^2_B	τ_E	R^2_E	N_B
Chorus	0.87 ± 0.05 hr	19.0 pT	0.97	2.90 ± 0.69 hr	0.55	19495
LBC	0.75 ± 0.04 hr	18.7 pT	0.96	5.16 ± 3.09 hr	0.48	14341
UBC	1.45 ± 0.18 hr	14.5 pT	0.47	2.97 ± 0.80 hr	0.49	10041

Table S3. Full chorus, LBC, and UBC magnetic (B) and electric (E) power spectral density decay timescales (τ) and peak wave magnetic field (B_w) for the dawn (6 to 9 MLT) region. We included error, R^2 values, and the number of statistics for the magnetic field measurements (N_B) to contextualize the quality of each fit.

Type	τ_B	B_w	R^2_B	τ_E	R^2_E	N_B
Chorus	2.13 ± 0.19 hr	16.4 pT	0.54	2.61 ± 0.35 hr	0.85	35161
LBC	1.74 ± 0.15 hr	16.5 pT	0.58	2.87 ± 0.51 hr	0.73	28233
UBC	16.57 ± 15.28 hr	11.9 pT	0.23	7.53 ± 3.20 hr	0.03	12478

Table S4. Full chorus, LBC, and UBC magnetic (B) and electric (E) power spectral density decay timescales (τ) and peak wave magnetic field (B_w) for the morning (9 to 12 MLT) region. We included error, R^2 values, and the number of statistics for the magnetic field measurements (N_B) to contextualize the quality of each fit.

Type	τ_B	B_w	R^2_B	τ_E	R^2_E	N_B
Chorus	3.72 ± 0.68 hr	18.9 pT	0.83	4.08 ± 0.87 hr	0.64	33133
LBC	4.27 ± 0.97 hr	19.3 pT	0.75	2.63 ± 0.42 hr	0.66	28816
UBC	2.35 ± 0.38 hr	12.3 pT	0.51	-3.61 ± 1.12 hr	0.12	9240

Table S5. Full chorus, LBC, and UBC magnetic (B) and electric (E) power spectral density decay timescales (τ) and peak wave magnetic field (B_w) for the afternoon (12 to 15 MLT) region. We included error, R^2 values, and the number of statistics for the magnetic field measurements (N_B) to contextualize the quality of each fit.

Type	τ_B	B_w	R^2_B	τ_E	R^2_E	N_B
Chorus	5.90 ± 1.49 hr	18.3 pT	0.34	-7.36 ± 2.52 hr	0.27	39868
LBC	5.27 ± 1.22 hr	18.3 pT	0.40	-5.70 ± 1.56 hr	0.46	38363
UBC	4.79 ± 1.63 hr	10.8 pT	0.58	4.72 ± 1.81 hr	0.30	5274

1.2 Figures

Table S6. Full chorus, LBC, and UBC magnetic (B) and electric (E) power spectral density decay timescales (τ) and peak wave magnetic field (B_w) for the evening (15 to 18 MLT) region. We included error, R^2 values, and the number of statistics for the magnetic field measurements (N_B) to contextualize the quality of each fit.

Type	τ_B	B_w	R^2_B	τ_E	R^2_E	N_B
Chorus	2.71 ± 0.35 hr	15.0 pT	0.25	1.35 ± 0.14 hr	0.67	14665
LBC	2.95 ± 0.42 hr	14.9 pT	0.22	1.27 ± 0.13 hr	0.69	14265
UBC	1.39 ± 0.45 hr	10.8 pT	0.07	3.75 ± 3.88 hr	0.03	937

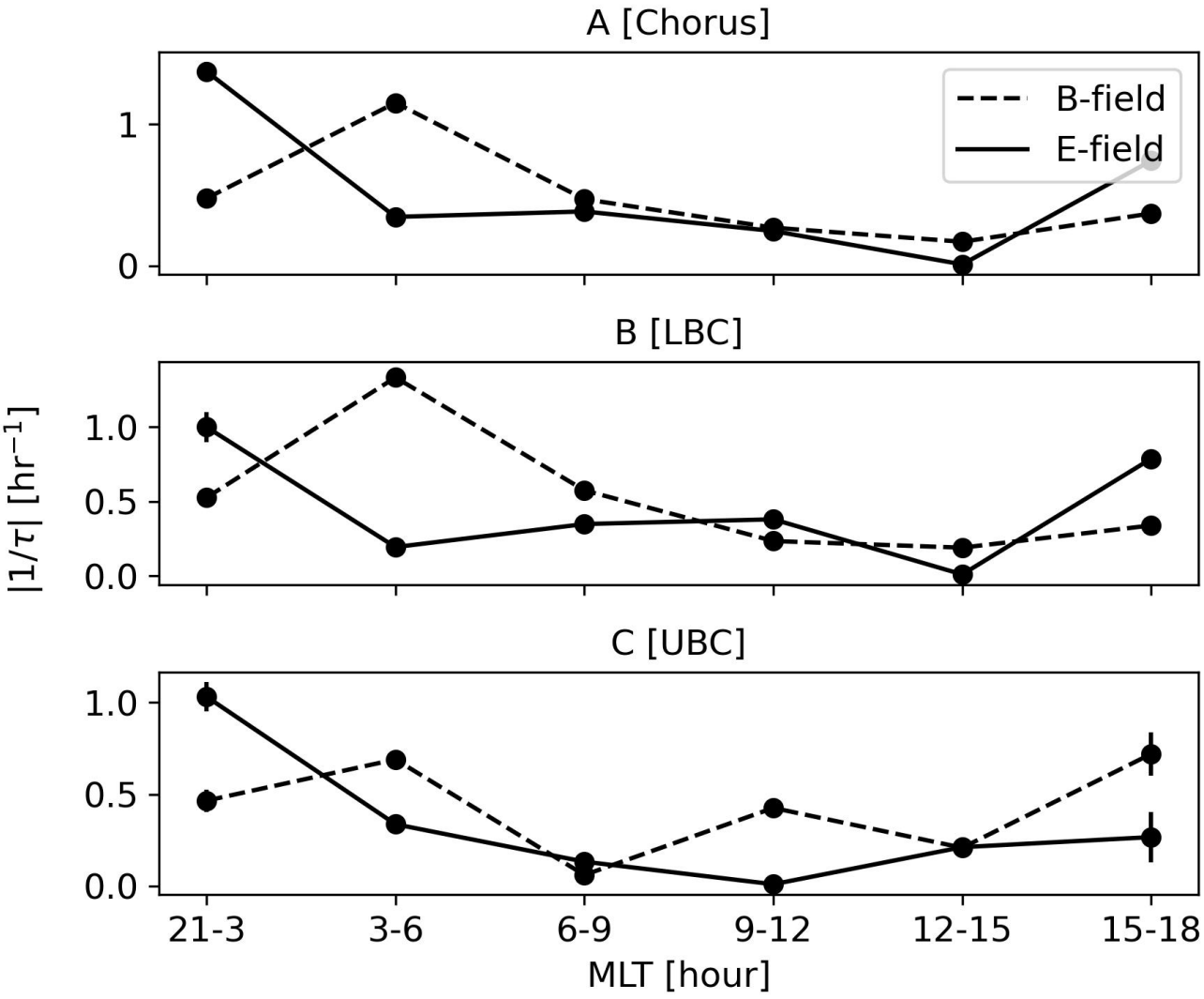

Figure S1. The inverse of magnetic (dashed) and electric (solid) field wave power decay timescales for the entire chorus range (Panel A), LBC (Panel B), and UBC (Panel C) versus MLT. For many of the points, the associated errors are smaller than the marker size. We combined the region 21 to 24 and 0 to 3 MLT and omitted 18 to 21 MLT due to statistical limitations.

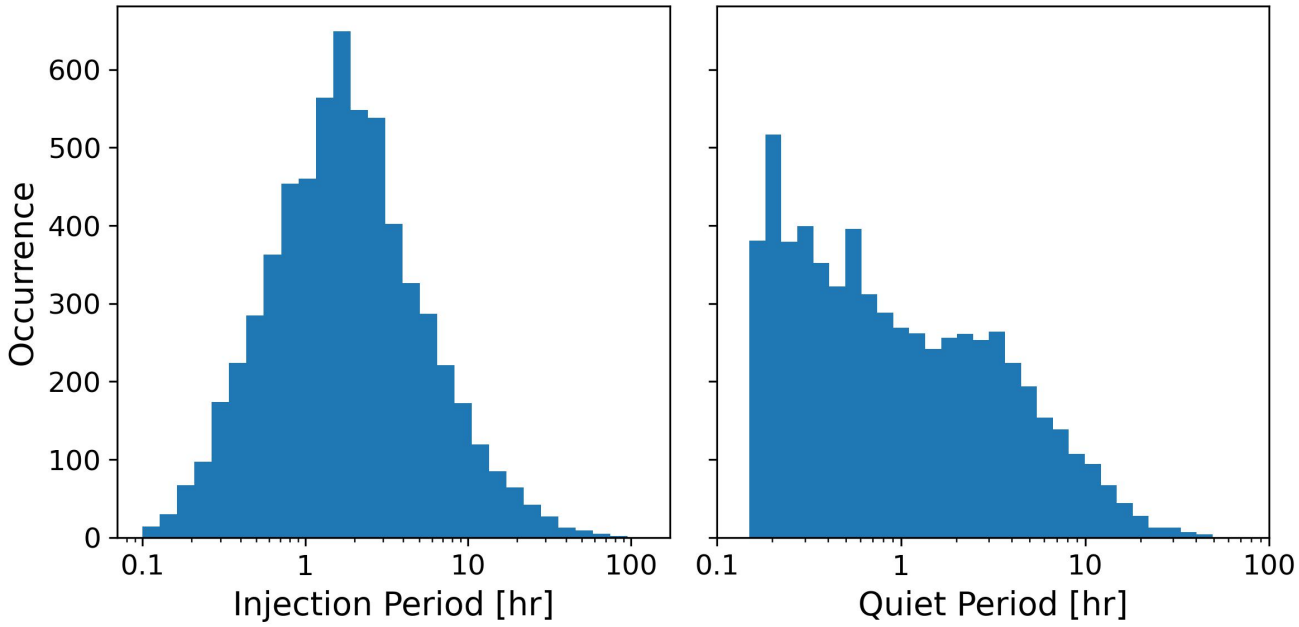

Figure S2. Histograms of injection period lengths and quiet period lengths as estimated from the SME index. See Section 2.2 in the main document for the specifics on how we estimated these.